Fast synchrotron X-ray tomography of dynamic processes in liquid aluminium alloy foam

By *Paul Hans Kamm, Francisco García-Moreno,* Tillmann Robert Neu, Korbinian Heim,*

Rajmund Mokso, John Banhart

[*]   *Dr. F. García-Moreno, P.H. Kamm, T. Neu,*

Institute of Applied Materials, Helmholtz-Zentrum Berlin für Materialien und Energie,

Hahn-Meitner-Platz 1, 14109 Berlin, Germany

E-mail: (garcia-moreno@helmholtz-berlin.de)

Prof. J. Banhart, Dr. K. Heim, Institute of Materials Science and Technology,

Technische Universität Berlin, Hardenberstr. 36, 10623 Berlin, Germany

Dr. R. Mokso, Swiss Light Source, Paul Scherrer Institute, 5232 Villigen PSI,

Switzerland

Abstract

The improvement of metal foam quality requires a deeper understanding of the fundamental mechanisms that act during foaming. X-ray tomography provides the 3D information needed to reveal the structural complexity of foams, but only recently temporal resolutions have become available that are sufficient to capture foam dynamics as well. Series of fast synchrotron X-ray tomographies are taken continuously at a rate of up to 5 Hz while aluminium alloy precursors are foamed in an X-ray transparent setup for several minutes using infra-red (IR) lasers for heating. The entire foaming process from the solid precursor to the expanded liquid foam is captured. The analysis of the sequence of tomographies is done with an emphasis on nucleation and bubble growth. In early stages of foaming, bubble and crack formation and evolution are observed. We analyze the nucleation stage and obtain quantitative results for the number of nucleation centers and their distribution and derive the nucleation rate as a function of time. Furthermore, we calculate the activation energy of the nucleation of bubbles.

1. Introduction

Solid aluminium foams are good candidates for a wide range of engineering applications owing to their low specific weight in conjunction with favourable mechanical and physical properties.[1] They have become an attractive research field both from the scientific viewpoint and the prospect of industrial applications. For further improvement of production methods an improved understanding of the fundamental mechanisms of foaming is crucial. However, the study of liquid metal foams is challenging due to the complex structure of foams in general and the conditions involved.[2] Especially gas nucleation, drainage, film stability and bubble coarsening govern the evolution of foam structure, but these are still not fully understood.[3] Cellular structures are usually investigated by imaging techniques such as light microscopy, SEM or X-ray tomography, although the information obtained is related to the solidified foam.[4] [5] Liquid metal foams, in contrast, have been characterized in-situ by 2D X-ray radioscopic analysis to study different dynamic processes.[6-8] Radioscopy, however, is more suitable for capturing the structure of foams in later stages of evolution, while the nucleation stage is hardly accessible and has therefore been mostly studied by ex-situ metallography or tomography.[9-11]

In this work, we report use of fast X-ray 3D tomography, also known as 4D tomography, recently available at the instrument "Tomcat" of the Swiss Light Source.[12-14] With its help we study fundamental questions of metal foam evolution in real time and in 3D for the first time. Via 4D tomography, we gain insights into the dynamics of the whole metal foaming process. We detect, separate and track all bubbles and other features in an emerging metal foam especially in the nucleation and early bubble expansion stage.

3

2. Experimental

An AlMg17.5 (in wt.%) alloy is chosen for the experiment. Pure Al and AlMg50 (in wt.%)

powders are mixed and hot-pressed uni-axially at 400 °C and 300 MPa for 15 min to achieve

a dense and gas-tight precursor. The AlMg50 acts as an intrinsic blowing agent in this alloy as

a high volume of gas is adsorbed in the powder.[15] The precursors of $(4 \times 4 \times 2)$ mm^3 size are

foamed inside a boron nitride (BN) crucible with an inner diameter of 8 mm at ~650 °C.

Heating is done by an efficient contactless infra-red (IR) laser heating system, see **Fig. 1.** The

crucible containing the sample rests on an Al_2O_3 tube that is connected to the rotation stage

and protects the stage from the evolving heat. The sample temperature is recorded and

controlled via a contactless pyrometer and calibrated by reference experiments in which the

melting point of pure Al precursors of the same size is approached and the emission

coefficient adapted accordingly.

The precursor is heated for about 100 s until reaching the foaming temperature of 650 °C and

kept at this temperature for another ~20 s. The foam already starts expanding after reaching

520 °C, roughly 40 s after the onset of the temperature reading shortly after starting to heat.

Image acquisition is either started after a selected temperature has been reached or the

imaging window is given by using a technique called post-event triggering, where images are

continuously stored and cyclically overwritten and the operator decides (based on life images)

when to stop image acquisition and saves the previously recorded images in the camera

memory. The first point of acquisition is defined as $t = 0$ s. During foam expansion, gas

nucleation and bubble growth takes place. At $t \approx 85$ s the lasers are switched off and the foam

starts cooling down.

The in-situ tomography experiments are performed at the Tomcat beamline of the Swiss Light

Source synchrotron facilities in Villigen, Switzerland. A pink X-ray beam irradiates the

sample. The transmitted radiation is converted into an optical image by a 100-μm thick

4

LuAG:Ce scintillator behind the sample. An optical system guides the image through a mirror to the CMOS sensor of a pco.dimax high speed camera (see Fig. 1). Each pixel on the camera corresponds to a square area of 3.16 µm size on the sample. This is sufficient to resolve the foam structure in good detail while allowing a temporal resolution for each individual tomography down to 0.2 s. To avoid artefacts caused by noise in the reconstructed images morphological opening is applied to the binarised volumes. This allows only bubbles with an equivalent diameter of at least ~11 µm to be evaluated. Under these conditions, we are able to evaluate the kinetics of foam evolution while avoiding blurring artefacts.

A series of tomographic projections with a region of interest covering almost the entire sample is directly recorded and stored in the camera memory, allowing for a continuous recording with a time resolution of 1 tomography/s (1 Hz) during ~100 s, i.e. covering the whole foaming evolution process. A more detailed analysis of the nucleation stage at a rate of 5 tomographies/s (5 Hz) during 10 s is performed to improve the time resolution in this important stage by using the already mentioned post event triggering. Due to the different triggering there is a shift of 2.2 s in the onset of acquisition between the two experiments.

The large number of tomographies recorded requires a special treatment including data handling, automatic reconstruction and evaluation algorithms for quantitative analyses. These were developed for this special purpose.

3. Results

The entire metallic foaming process comprising the expansion, holding and cooling stages is recorded in-situ over a period of 100 s via fast tomography. The time resolution is set to 1 Hz, i.e. 1 tomography/s. Representative tomographic reconstructions showing the evolution of the bubble structure (actually the surfaces of bubbles) of an AlMg17.5 foam at different times ($t =$ 2, 20, 40, 60, 80 and 100 s) are shown in **Fig. 2**. At $t = 2.2$ s, when expansion starts, small and equally distributed bubbles with a mean equivalent diameter of ~30 µm are observed. During

the first ~20 s, further bubbles nucleate and the already existing ones grow in size and, therefore, foam volume increases accordingly. During these first 20 s of foaming the system undergoes the most pronounced structural changes, which will be presented later in more detail. In the interval $t = 20-40$ s, the foam contains a mixture of small bubbles (< 0.1 mm), larger bubbles (> 0.1 mm) and some large connected regions (resembling cracks) and evolves slowly towards an increasingly coarser foam. From $t = 40-80$ s, some bubbles reach a diameter of up to 1 mm and, in general, the large bubbles become rounder and more defined. The foam develops its typical structure. In the final 20 s, some bubble surfaces become corrugated in the course of shrinkage by cooling.

The temperature and porosity evolution calculated from the tomographies is plotted in **Fig. 3**. After the initial fast expansion, we observe a stagnation of the maximum porosity at around 40−45 % from $t \approx 40$ s to $t \approx 85$ s, after which the heating power is switched off and the foam starts shrinking. The hatched region in Fig. 3 represents the temporal range studied by in-situ tomography in this work.

To gain a more detailed view of the temporal evolution in the nucleation stage another experiment with a tomography repetition rate of 5 Hz is carried out and the first 10 s of foaming are recorded, corresponding to the region indicated in the inset in Fig. 3. We assume that in the early stage ($t = 0-6$ s) the number of bubbles detected corresponds to the number of gas nuclei in the foam, as the ratio between their mutual distance to their diameter is too large to expect any interaction such as coarsening or coalescence. In fact, none of these effects could be found at this stage, thus corroborating the assumption. Therefore, from the total number of bubbles as a function of time we can determine the nucleation rate as presented in **Fig. 4**. Here we observe that the number of bubbles increases over the first 10 s and the nucleation rate has a maximum of $9.5 \cdot 10^4$ cm^{-3}s^{-1} at $t = 7.6$ s.

Fig. 5 shows the mean equivalent bubble diameter and its standard deviation as a function of time and in the inset its corresponding distributions during the nucleation stage. A clear shift of the bubble size from 20 μm to 75 μm during the first 10 s of foaming in conjunction with a wider size distribution is visible.

The anisotropy of the bubbles, described by 1 minus the ratio of the smallest to the largest eigenvalue of the bubble's covariance matrix, denoting the deviation from a spherical shape (where a value of 0 points at a more spherical object and a value close to 1 either at elongated or flat objects), is given in **Fig. 6** for almost the entire foaming period of 100 s. After a strong increase in anisotropy during the first 15 s the graph splits into bubbles whose shape is changing back towards spherical until $t \approx 60$ s and remain spherical until the end of the process and a fraction of deformed bubbles whose anisotropic shape persists till the end.

4. Discussion

4D tomography is demonstrated to be a very powerful characterization method providing a range of options to analyse dynamic processes such as foaming. These analyses are only possible at a highly brilliant X-ray source such as the third-generation SLS. A scintillator with a high light efficiency and a short latency time combined with a state-of-the-art high-speed camera are requested to capture so many radiographs in a short time. Finally, a lot of effort has to be put into data handling and processing. Considering that each tomography involves >1 GB of data and hundreds of tomographies are taken, the development of automatic reconstruction and evaluation algorithms for quantitative analyses is mandatory.

In selecting the best imaging conditions, a good compromise between spatial and time resolution has to be sought: image acquisition has to be quick enough to follow the evolution of the foam, but slow enough to limit the amount of data that has to fit into the camera memory and that increases sharply with increasing spatial resolution. A given spatial and

7

temporal resolution then defines the period of tomographic imaging. This is the reason for the selected time resolution of 1 Hz for the imaging of the whole foaming stage (100 s) and 5 Hz for the nucleation stage (10 s) where most changes occur and on which interest is focused in this study. We were able to address all these optimization issues and gain new insights into liquid metal foam evolution. Both experiments are in very good agreement during the period they overlap as seen in Fig. 3 for the porosity evolution.

Assuming a uniform foam expansion, which is likely due to the good thermal conductivity of the precursors,[15] the porosity evolution of the subvolume given in Fig. 2 and Fig. 3 reflects the expansion curves of the entire sample as known, e.g., from radioscopy experiments.[16] The co-existence of near-spherical bubbles with large and corrugated voids in an intermediate stage from ~20−40 s is the consequence of cracks that are formed in the alloy. Although the temperature increases from ~555 °C to ~595 °C in the period $t = 20$ s to 40 s and the eutectic temperature of AlMg17.5 is nominally 450 °C, the alloy is not fully liquid since the precursor consists of pure Al blended with AlMg50 powder. This implies that the system needs time for diffusion to establish the nominal composition everywhere, which is not available under the conditions of the current experiment. This explains the occurrence of large non-spherical objects. Later, between $t \approx 40$ s and 100 s, some of the large bubbles continue to grow and show a typical foam coarsening behavior over time.[17,18] Some of the large bubbles also rupture after a certain time in the course of foam ageing. In this period, corrugated bubbles appear. It is evident from the sequence of tomographies that these correspond to ruptured large bubbles, the oxidized surfaces of which cannot be reabsorbed by the molten liquid phase, thus giving rise to irregular cavities.

Fig. 4 corroborates the finding that over the first 10 s new nuclei appear and previously nucleated bubbles further grow, thus leading to the wider size distribution in Fig. 5. In Fig. 6, the anisotropy during the first 6 s is low (0.2) and corresponds to the initially round bubbles.

8

The following increase of bubble anisotropy from 0.2 to 0.9 until $t \approx 15$ s, which still concerns only small bubbles, is due to incipient coalescence, where two neighboring bubbles first merge to an elongated bubble and regain their spherical shape later. This is shown in **Fig. 7** for the temporally higher resolved experiment where between $t = 6.6$ and 6.8 s one of the first occurring coalescence events is shown.

For $t > 15$ s, nucleation seems to be so strong and the precursor so weak that its yield strength does not withstand the nucleation pressure and larger cracks form all over the sample in soft but still partially solid regions. This leads to non-spherical pores. This is a well-known effect during metal foaming and undesirable as it leads to large bubbles and non-uniform foam structures.[9, 10] These cracks are the reason for the splitting of the anisotropy of bubbles plotted in Fig. 6. The effect also leads to a kink in the porosity evolution curve at $t \approx 20$ s in Fig. 3 indicating an acceleration of foam expansion.

The detailed analysis of the first 10 s of foaming clearly reveals the process of bubble nucleation and growth and allows us to follow and quantify the number, size, shape, etc. of bubbles during foaming as shown in Fig. 4. The maximum of the nucleation rate found at $t = 7.6$ s can be explained by the large number of bubbles (> 1000) which start touching each other and coalesce after $t = 6.6$ s. By displaying the mean equivalent bubble diameter against the square root of time we find a linear dependence in the range of $t = 5-10$ s with a mean equivalent diameter of ~60 µm at $t = 7.6$ s (Fig. 5). Mathematical models for nucleation and growth in early stages described for polymeric foams predict such behaviour.[19,20] These models take into account the diffusion mass transfer of the limited, dissolved gas in an influence volume around a bubble, thus predicting a limited bubble growth evolution proportional to the square root of time.

Classical nucleation theory models the nucleation rate as an Arrhenius law.[21] The number of critical nuclei formed per unit time and volume can be written as:[22]

$$\dot{n}_{\text{het}} = f_1 A \exp\left(\frac{-W f(\theta)}{k_B T}\right), \tag{1}$$

with the heterogeneous nucleation rate $\dot{n}_{\text{het}}$, frequency factor f_1, concentration of

heterogeneous nucleation sites A, Boltzmann's constant k_B, temperature T, the energy barrier

for homogeneous nucleation W and a function of the wetting angle θ reducing the energy

barrier for heterogeneous nucleation. Fig. 8 shows the logarithm of the nucleation rate taken

from Fig. 4 as a function of reciprocal temperature thus depicting an Arrhenius plot. The slope

obtained for $t < 6.6$ s allows us to calculate a value for the energy barrier a nucleus has to

overcome to become stable. For this alloy, we calculate the corresponding energy barrier

$Wf(\theta) \approx 2\times10^{-18}$ J. For this calculation we have to assume that all bubbles are gas nuclei and

no coalescence occurs in the time/temperature range considered. As $f(\theta)$ is unknown and the

data is taken from a non-isothermal experiment this value should be treated as a rough

estimate for the order of magnitude of the nucleation activation energy.

5. Conclusions

- Fast in-situ tomography of the dynamic foaming process of an aluminium alloy is performed for the first time. This method offers us new perspectives in understanding foam evolution.
- A deeper insight into the nucleation process can be achieved. Different states of nucleation are observed.
- The nucleation rate is measured and found to peak after a few seconds of foaming. The energy barrier for bubble nucleation can be estimated.

6. Outlook

We expect to get a more precise numbers for nucleation centers, rate, energy and bubble size distribution and evolution in dependence of the precursor compaction method or the composition of the alloy by applying higher acquisition rates. Additionally, phenomena such as bubble ruptures, bubble movements or collapse can be also studied with this method quantitatively, allowing to extend the knowledge about foam development and foam structure.

FIGURES
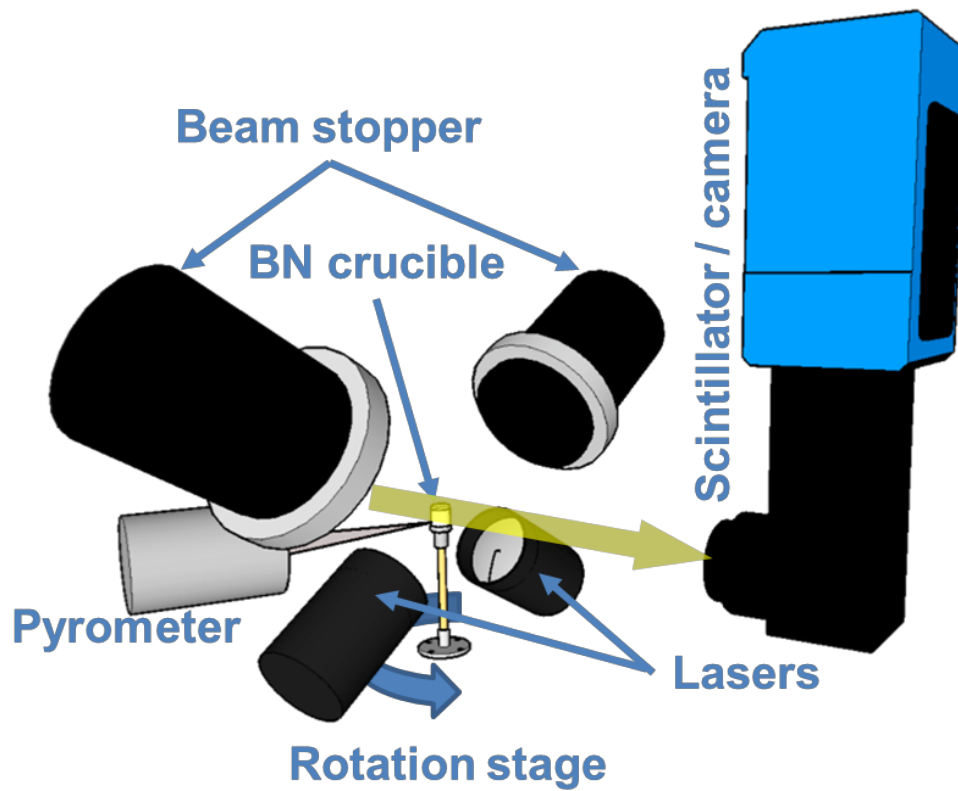
Fig. 1. Sketch of experimental setup: The sample is placed in a BN crucible which is heated by two IR lasers with their corresponding beam stoppers. The temperature is recorded by a pyrometer. The sample is rotated and a detector system composed by a scintillator screen, optic and CMOS camera records the transmitted X-ray beam (bold arrow).
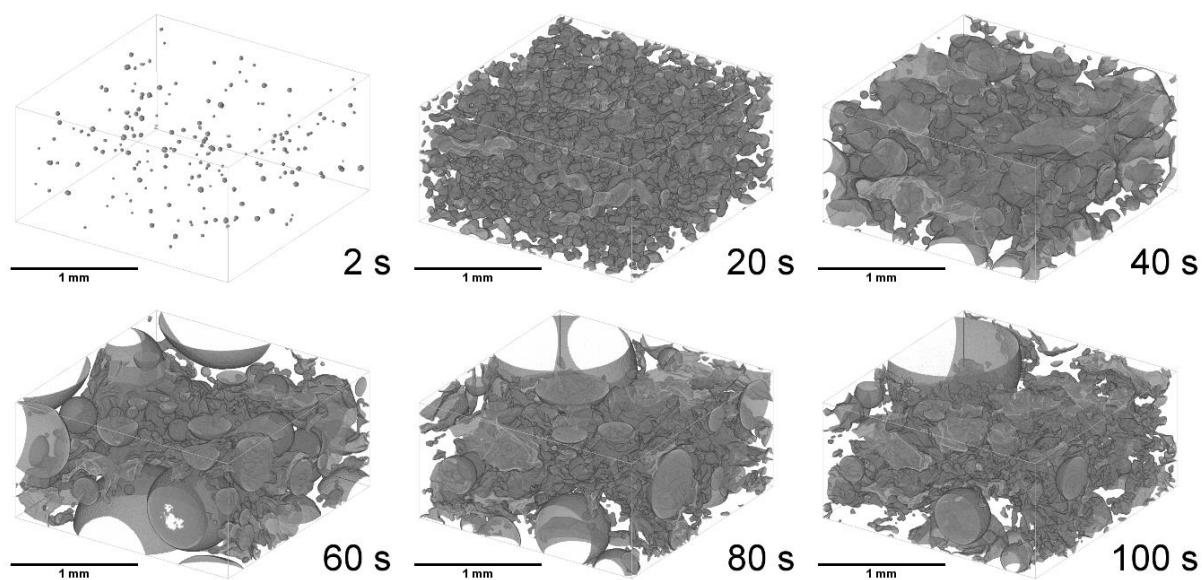
Fig. 2. Tomographic reconstructions (subset of entire volume) of the bubble structure of AlMg17.5 alloy foamed at 650 °C. Specific times are selected, namely t = 2, 20, 40, 60, 80 and 100 s after the onset of foaming. Bubble evolution is clearly observable.
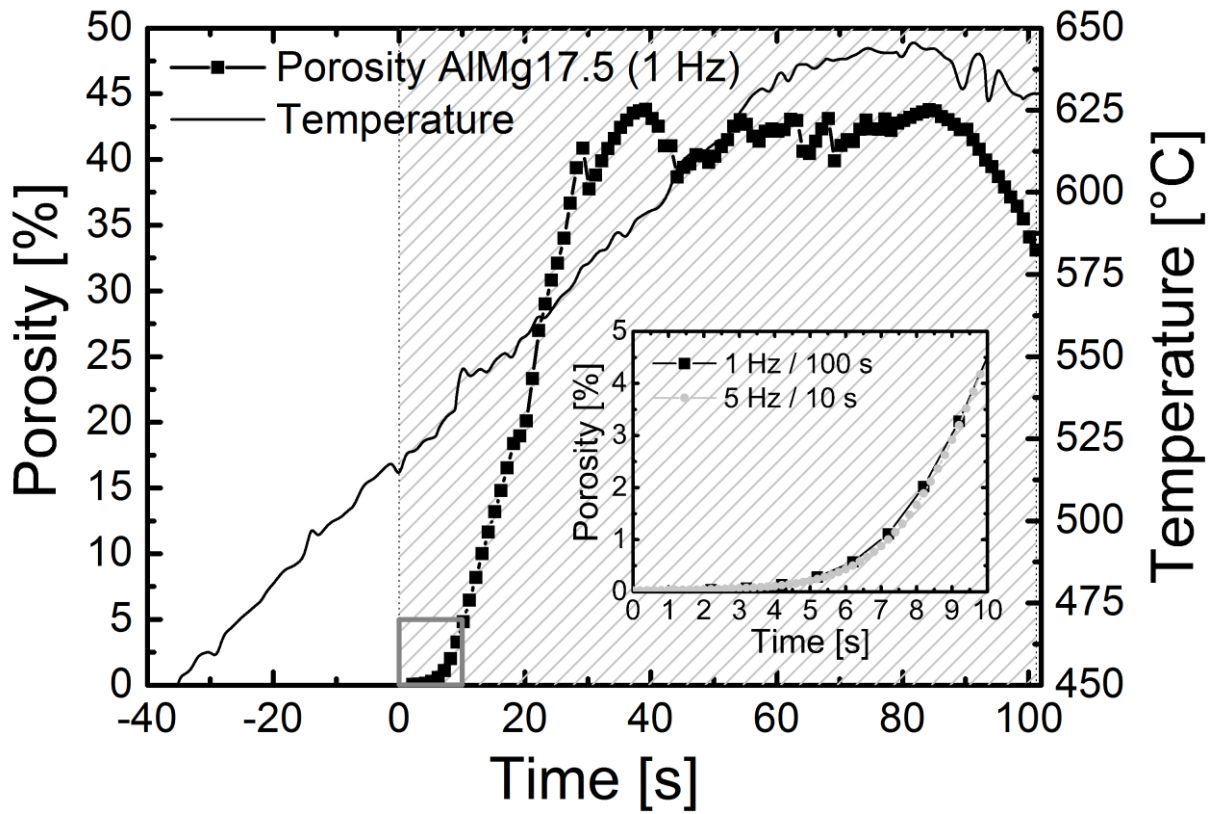
Fig. 3. Temperature and porosity evolution during foaming. *t* = 0 s refers to the onset of foam expansion and earliest recording. The inset shows the first 10 s of nucleation for the higher temporal resolution (dots). The plot for the 1 Hz experiment (squares) is shifted by 2.2 s to compensate slight offsets between the two experiments and to match the porosity evolution.
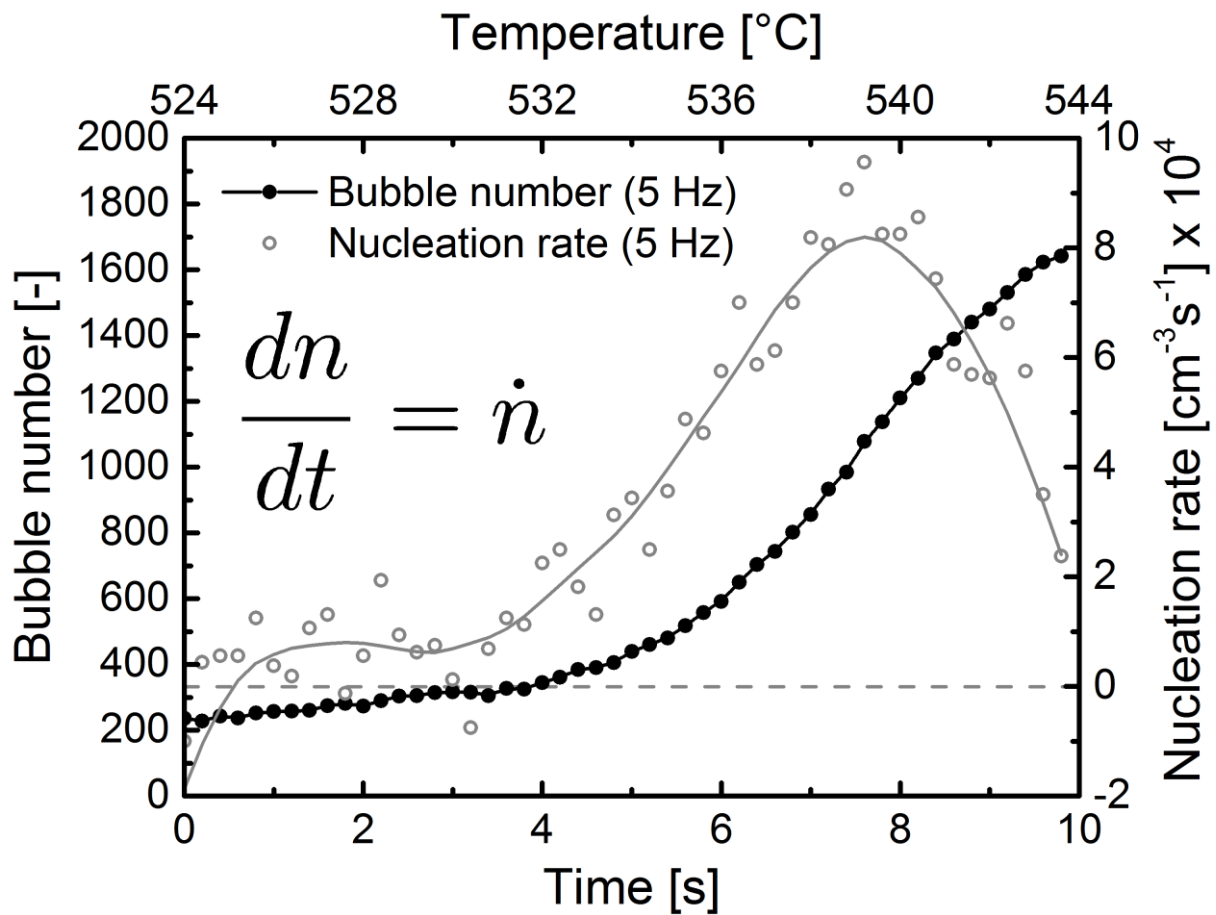
Fig. 4. Temporal evolution of the number of bubbles and the corresponding nucleation rate in the first 10 s of foaming derived from a 5 Hz tomography experiment. Data corresponds to the inset in Fig. 3.
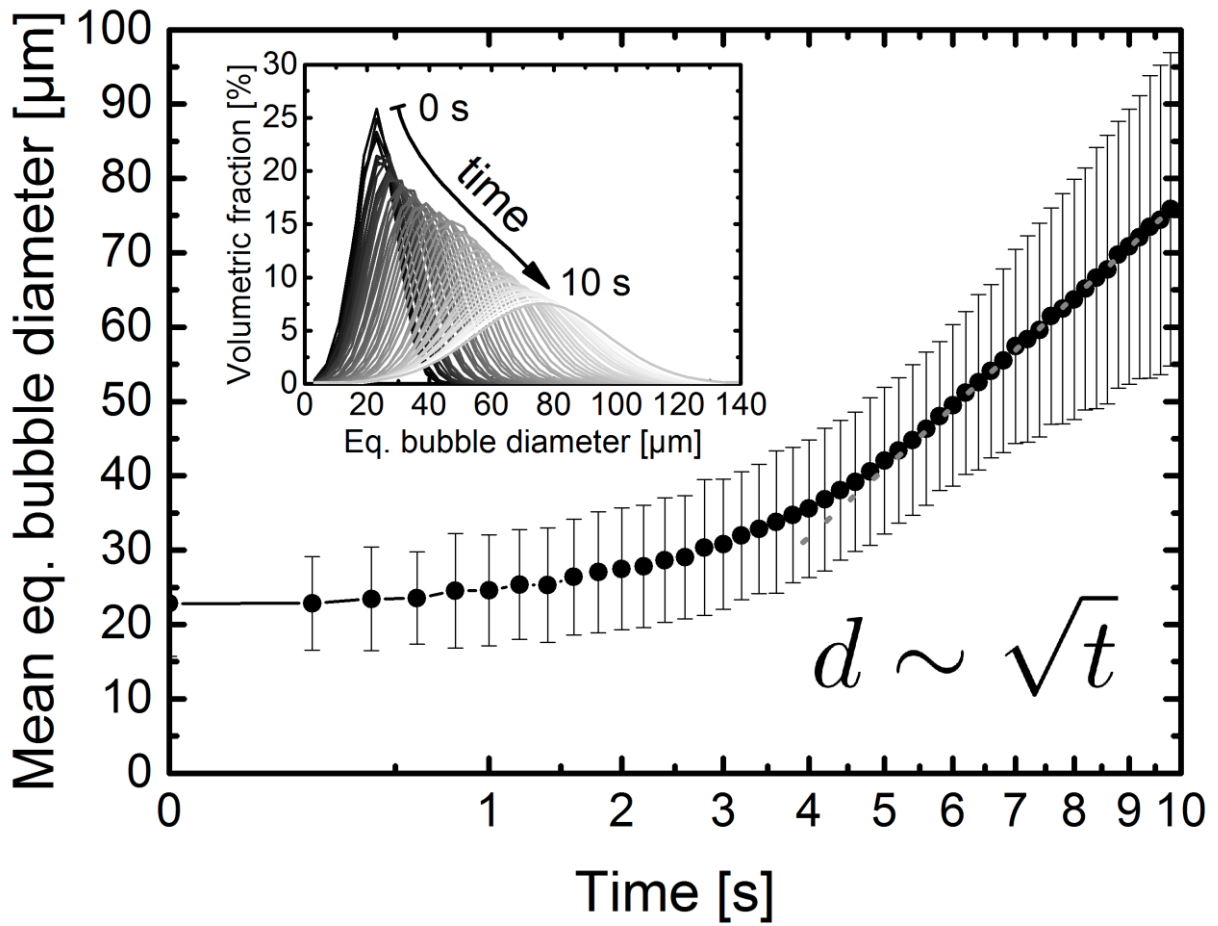
Fig. 5. Mean equivalent bubble diameter evolution displayed against the square root of foaming time and

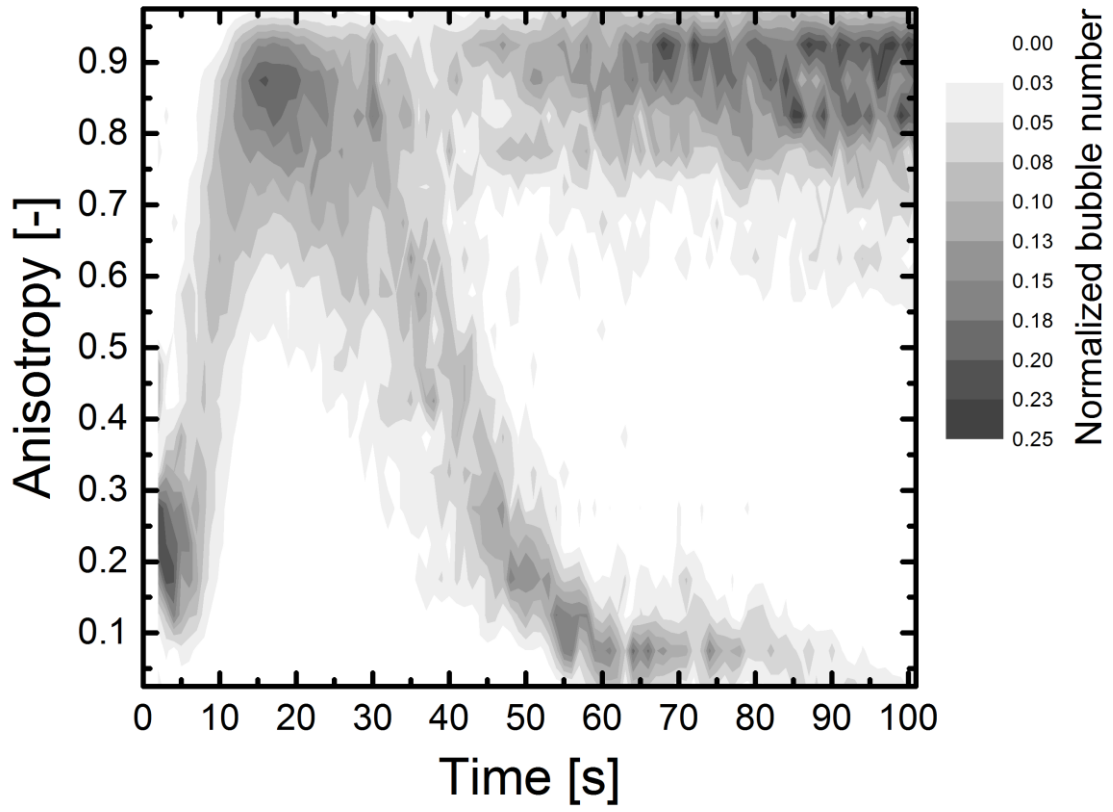corresponding bubble size distribution fits (inset) during the nucleation stage

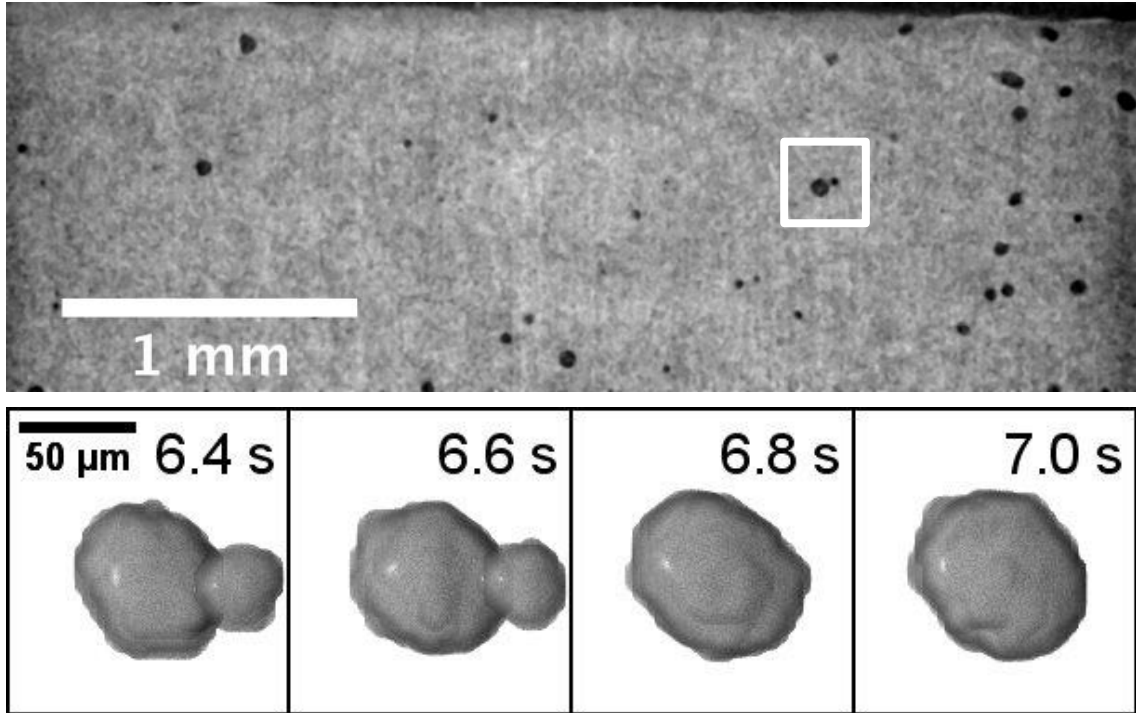**Fig. 6. Anisotropy (deviation from a spherical shape) of bubbles over foaming time.**

Fig. 7. Vertical slice of a reconstructed tomography at *t* = 6.6 s (top) and 3D rendering of one of the first observed coalescence events of two pores in four subsequent time steps (bottom).
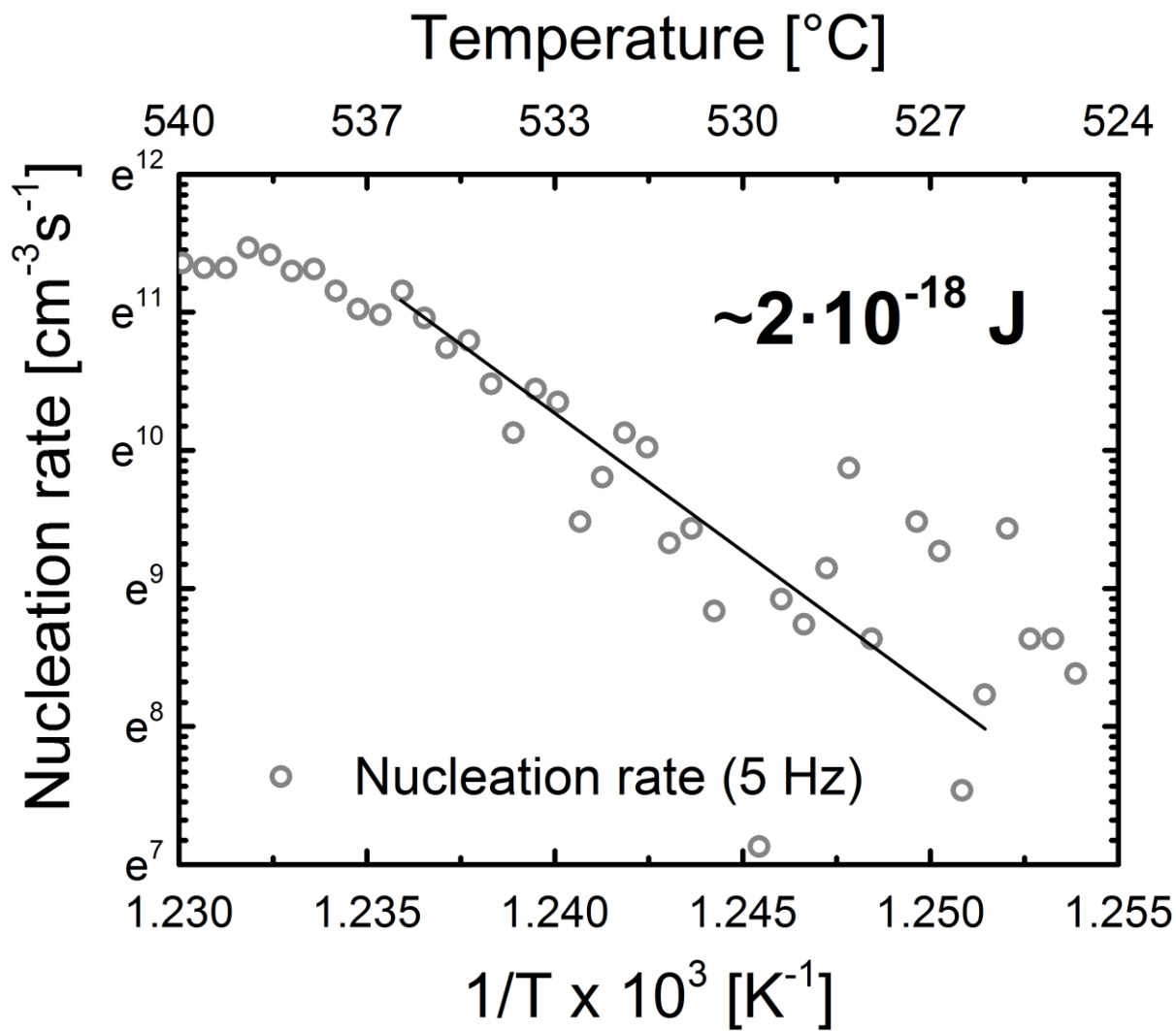
Fig. 8. Arrhenius plot of the nucleation rate against 1/T.

References

[1] F. García-Moreno, *Materials* **2016**, *9*, 85.

[2] J. Banhart, D. Weaire, *Phys. Today* **2002**, *55*, 37.

[3] A. Haibel, A. Rack, J. Banhart, *Appl. Phys. Lett.* **2006**, *89*, 154102.

[4] V. Gergely, B. Clyne, *Adv. Eng. Mater.* **2000**, *2*, 175.

[5] M. Kolluri, M. Mukherjee, F. Garcia-Moreno, J. Banhart, U. Ramamurty, *Acta Mater.* **2008**, *56*, 1114.

[6] F. Garcia-Moreno, E. Solorzano, J. Banhart, *Soft Matter* **2011**, *7*, 9216.

[7] F. Garcia-Moreno, C. Jimenez, P. H. Kamm, M. Klaus, G. Wagener, J. Banhart, C. Genzel, *J. Synchr. Radiat.* **2013**, *20*, 809.

[8] A. Rack, F. Garcia-Moreno, T. Baumbach, J. Banhart, *J. Synchr. Radiat.* **2009**, *16*, 432.

[9] L. Helfen, T. Baumbach, H. Stanzick, J. Banhart, A. Elmoutaouakkil, P. Cloetens, *Adv. Eng. Mater.* **2002**, *4*, 808.

[10] L. Helfen, T. Baumbach, P. Pernot, P. Cloetens, H. Stanzick, K. Schladitz, J. Banhart, *Appl. Phys. Lett.* **2005**, *86*, 231907.

[11] A. Rack, H. M. Helwig, A. Bütow, A. Rueda, B. Matijašević-Lux, L. Helfen, J. Goebbels, J. Banhart, *Acta Mater.* **2009**, *57*, 4809.

[12] K. Mader, R. Mokso, C. Raufaste, B. Dollet, S. Santucci, J. Lambert, M. Stampanoni, *Colloids Surf., A* **2012**, *415*, 230.

[13] R. Mokso, D. A. Schwyn, S. M. Walker, M. Doube, M. Wicklein, T. Müller, M. Stampanoni, G. K. Taylor, H. G. Krapp, *Scientific Reports* **2015**, *5*, 8727.

[14] E. Maire, C. Le Bourlot, J. Adrien, A. Mortensen, R. Mokso, *Int. J. Fract.* **2016**, *200*, 3.

[15] M. Mukherjee, F. Garcia-Moreno, C. Jiménez, J. Banhart, *Adv. Eng. Mater.* **2010**, *12*, 472.

20

[16]   F. Garcia-Moreno, M. Fromme, J. Banhart, *Adv. Eng. Mater.* **2004**, *6*, 416.

[17]   A. Saint-Jalmes, *Soft Matter* **2006**, *2*, 836.

[18]   A. Stocco, F. Garcia-Moreno, I. Manke, J. Banhart, D. Langevin, *Soft Matter* **2011**, *7*,

631.

[19]   M. Amon, C. D. Denson, *Polym. Eng. Sci.* **1984**, *24*, 1026

[20]   M. A. Shafi, K. Joshi, R. W. Flumerfelt, *Chem. Eng. Sci.* **1997**, *52*, 635.

[21]   M. Volmer, A. Weber, *Z. Phys. Chem.* **1926**, *119*, 277.

[22]   J. S. Colton, N. P. Suh, *Polym. Eng. Sci.* **1987**, *27*, 485.